A mascon approach to estimating the depth of Jupiter's Great Red Spot with Juno gravity measurements

Marzia Parisi[a,*], William M. Folkner[a], Eli Galanti[b], Yohai Kaspi[b], Dustin R. Buccino[a], Kamal Oudrhiri[a], Scott J. Bolton[c]

[a] *Jet Propulsion Laboratory, California Institute of Technology, Pasadena, California 91109, USA*
[b] *Department of Earth and Planetary Sciences, Weizmann Institute of Science, Rehovot 76100, Israel*
[c] *Southwest Research Institute, San Antonio, Texas 78238, USA*

Abstract

We evaluate a new method for determining the depth of Jupiter's Great Red Spot (GRS) with two *Juno* overflights optimized for gravity science. The small-scale, localized nature of the anticyclone requires a detection method where the gravity perturbations are regional. To this end, we model the GRS as a dipole of flat disk mascons, separated along the radial direction of Jupiter. This structure is supported both by thermal wind balance and Juno microwave observations of the GRS. Furthermore, the mascon approach is suitable for multiple flybys as it can account for the vortex's drift with respect to Jupiter System III. We present the results of both a covariance analysis and a recovery analysis of the simulated data, in terms of accuracy in the estimation of the GRS mass and depth of winds through precise Doppler tracking of the Juno spacecraft. We find that the detection of the GRS is possible using both gravity passes, if the surface dynamics extend at least several hundred kilometers below the cloud tops. Moreover, the analysis highlights the possibility of discriminating the vertical dipole structure from models featuring a different number or location of the mass concentrations.

Keywords: Great Red Spot, Juno, Gravity Science, Jupiter, Atmospheric Dynamics, Orbit Determination

*Corresponding author

Declarations of interest: none.

1. Introduction

The Great Red Spot (GRS) is an outstanding feature of Jupiter's atmosphere and the target of extensive observations since the late 1800s. The vortex is embedded in the strong Jovian zonal jets, and drifts with respect to the uniform rotation (System III). The physical appearance and characteristics of the anticyclonic storm are continuously changing, with recent observations concluding that its transition from elliptical to circular shape is progressing with an approximately linear trend [28]. The Juno mission enabled considerable advances in the study of the GRS rich dynamics [26], however the question concerning the depth of the vortex still stands. On a larger scale, it has been long debated whether Jupiter's strong zonal winds that are visible at the cloud level are shallow or deep [4, 12, 30]. Juno provided an answer to this long-standing question by measuring the asymmetric gravity field of the planet [10], and concluded that the zonal winds must extend a few thousand kilometers below the cloud level to explain the measured odd gravity signal [17]. It is still unknown whether the GRS is as deep as the zonal winds or characterized by a different scale height. It has been argued that the vortex is shallow and constrained to a thin weather layer despite its long lifespan [6, 20]. Others have argued that the vortex longevity can only be explained by deep roots extending into the interiors [32]. To date, the only Juno overflight of the GRS occurred on 11 July 2017 (labeled as PJ07, short for perijove 7) and was optimized for Microwave Radiometer (MWR) observations, which measured the vortex's thermal emission, penetrating down to a few hundred bars, about 350 km below the surface. The instrument observed colder than average brightness temperature anomalies in the upper levels and warmer anomalies at depth, highlighting a sign inversion of the temperature perturbation [19], which is akin to a dipole structure. What happens below a few hundred kilometers is still a mystery.

The upcoming Juno science orbits over the GRS, scheduled for February (PJ18) and July 2019 (PJ21), are optimized for gravity science and provide the next opportunity to observe the storm and determine its depth. The detection of the GRS gravity signal using Juno data was proposed by Parisi et al. [23], whose analysis considered a single close flyby of the GRS. The method relied on spherical harmonics, as the GRS makes up for a large part of the predicted non-axially symmetric gravity field. They concluded that the gravity signal of the GRS could be detected with a single overflight only if the vortex was deeper than 2,000 km, since a 30x30 tesseral field was needed to define accurately the GRS gravity signal. In the present work, we resort to a different model to describe the concentrated mass anomalies expected from the vortex circulation. Mascons are mass concentrations that were first defined in Muller & Sjogren [21]. They can assume different shapes and their use is particularly apt for solid bodies, for instance they have been used for the analysis of gravity data from the GRACE [13] and GRAIL [33] missions. In 1976, Null [22] attempted to estimate the mass concentration of the GRS with *Pioneer* 10 and 11 radiometric data. He adopted a single mascon model and by combining the two encounters with Jupiter he concluded that the effect of the vortex on range-rate measurements was negligible at such distances (2.8 and 1.6 Jupiter's radii, respectively). In 2019, Juno will fly twice over the GRS within 20,000 km, opening up the possibility for the detection of its anomaly with gravity measurements, and define its deep structure. The purpose of this work is to link the estimation of the mascon masses, accompanied by the expected accuracies, to the vortex's depth. The objective is achieved by means of a covariance analysis and a recovery analysis.

This paper is structured as follows. In Section 2 we introduce the thermal wind model, used to relate Jupiter's turbolent surface winds around the GRS to the expected gravity anomalies. In Section 3 we define a model of the vortex as a dipole of disk mascons. In Section 4 we report the results of the covariance and recovery analyses in terms of formal uncertainties in the estimation of the GRS mass anomalies. In Section 5 we present our conclusions and discuss the validity and limitations of our method for the determination of the GRS depth

with Juno gravity data.

2. The wind-gravity relation

The thermal wind (TW) equation has been widely used in the past to explain Jupiter's large-scale dynamics ([14, 15]) and the gravity field derived from the density anomaly profile has matched with remarkable accuracy the values of the first four odd harmonics of Jupiter's gravity field [17]. Kaspi et al. [17] were able to invert the observed asymmetric gravity field into a wind field by using an optimization based on the adjoint method [9]. Similarly, assuming that, to first order, the dynamics of the GRS are geostrophic, the TW model can be used to predict the density anomalies associated with the strong anticyclonic flow [23]. The atmosphere of Jupiter is rotating differentially with surface velocities that are known from multi-spectral observations of the atmosphere during the *Cassini* Jupiter flyby in December 2000 [5]. Panel a of Figure 1 shows the magnitude of the wind speed around the GRS location, within an area of 24° in latitude and 34° in longitude, after removing the zonal average from Equation (1), to highlight the azimuthal variations of the winds characteristic of the GRS [23]. The velocities of the vortex walls reach magnitudes of up to 90 ms^{-1} with respect to the background zonal flows [5]. The north-south velocity profile is asymmetric with respect to latitude 20°S, with the northern edge of the collar characterized by higher wind speeds than the southern edge. The eastward longitude of the GRS geometric center in Jupiter System III was 274° in December 2000, at the time of the Cassini flyby. However, the GRS drifts westward relative to System III by about 0.36 degrees per day [28].

Similar to Kaspi [16], Parisi et al. [23] and Kaspi et al. [17], we propagate the surface velocity profile downwards along cylinders and assume an exponential decay in the radial direction by choosing the scale height H:

$$\begin{aligned} u\left(r,\theta,\phi\right) &= u_{\mathrm{cyl}}\left(r,\theta,\phi\right) e^{-\frac{R_J - r}{H}}, \\ v\left(r,\theta,\phi\right) &= v_{\mathrm{cyl}}\left(r,\theta,\phi\right) e^{-\frac{R_J - r}{H}}, \end{aligned} \tag{1}$$

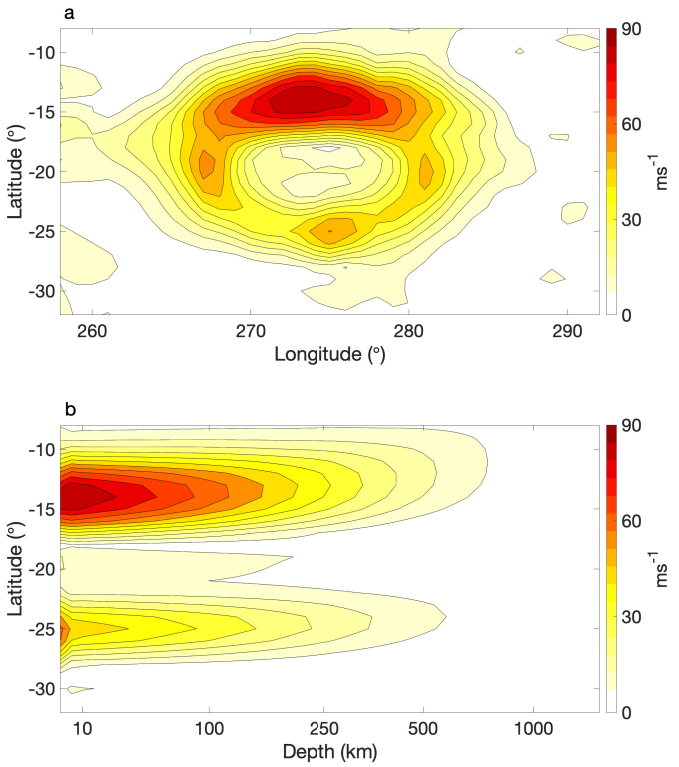

Figure 1: Panel a: magnitude of the GRS velocity at the cloud level in Jupiter System III (in ms^{-1}), as seen by Cassini in the year 2000 [5]. The winds that constitute the external walls of the GRS are rotating anticlockwise. Panel b: magnitude of the GRS winds as a function of depth, for H=300 km. Vertical section along the GRS longitude at the time of the Cassini flyby (274°E).

where u is the azimuthal component of the velocity (east-west), v is the meridional component (north-south) and r, θ, ϕ are respectively the distance from the center of the planet, latitude and longitude in Jupiter System III. The functions $u_{\mathrm{cyl}}, v_{\mathrm{cyl}}$ are obtained by propagating the wind speed components, as measured at the cloud level [5], along the spin direction [14, 27]. R_J is Jupiter's mean radius. Panel b of Figure 1 shows the wind speed as a function of depth, for H=300 km, along the radial direction of Jupiter at a fixed longitude (274°E).

The TW equation relates the velocity profile of a fluid to density anomalies, assuming that the horizontal pressure gradients are balanced by the Coriolis force in the momentum conservation. This assumption is valid for Jupiter, as the Rossby number is small because of its fast rotation and large scales [24]. The equation is [14]:

$$2\boldsymbol{\Omega} \cdot \nabla (\tilde{\rho}\boldsymbol{v}) = \nabla\rho' \times \boldsymbol{g}, \tag{2}$$

where $\boldsymbol{\Omega}$ is Jupiter's mean rotation rate (corresponding to a period of ≈9h 55m 30s), $\boldsymbol{v}$ is the velocity vector and $\boldsymbol{g}$ is the radial gravity vector. The density is composed of a static component $\tilde{\rho}(r)$ and small anomalies related to the dynamics $\rho'(r, \theta, \phi)$. The latter are linked to the dynamics of the atmosphere and are much smaller than the former. In this analysis we assume that the effect of the oblateness of the planet in Equation (2) is negligible, since this contribution is of second order in the description of the large-scale dynamics of Jupiter [8].

3. The Great Red Spot dipole model

Equation (2) can be broken into a system of scalar equations and solved numerically for ρ' over a horizontal grid of 24°x34° and 87 non-equally spaced vertical levels, given the wind profile in Equation (1) and the radial gravity vector [23]. The structure of the density perturbations at the GRS location (called henceforth Finite Element model) is revealed by showing a vertical section of the planet at longitude 274°E (Figure 2, panels a and b). For H=300 km (panel a) the density anomaly reaches a maximum positive value of 0.016 kgm^{-3} at a depth of 260 km, while changing sign and reaching a maximum negative value of -0.006 kgm^{-3} at 1,000 km depth. For H=1,000 km (panel b), the peak values of the density contrast are 0.05 kgm^{-3} and -0.02 kgm^{-3} at depths of 800 km and 2,400 km respectively. In both cases, the GRS density anomalies are structured as a dipole in the radial direction, positive closer to the cloud top and negative at depth. The anti-cyclonic circulation causes a mass up-welling at

higher altitudes, and a mass deficiency at depth. The density profile obtained by integrating the TW equation is defined short of a constant of integration which is a function of the radial distance r. The constant can assume different values at different radial levels and produce different density profiles from the ones in Figure 2. However, the Juno Doppler data is sensitive to variations in the mass density along its flight path with respect to the background density. In view of this, if we consider the density gradient on each horizontal level, then its profile as a function of depth is independent of the constant of integration. To understand the physics behind the dipole structure we must consider the radial derivative ($\frac{\partial}{\partial r}$) of the term $\nabla(\tilde{\rho}\boldsymbol{v})$ in Equation 2. While the hydrostatic density increases with depth, the velocity decreases exponentially along the radial direction. These opposite effects are responsible for the change of sign in the density anomaly ρ'. Specifically, the background density gradient sets the overall positive radial gradient in the upper levels of the atmosphere, while the negative wind gradient dominates at depth.

The vertical mass dipole structure is also supported by Juno MWR observations of the GRS deep structure, obtained by measuring the thermal emission from Jupiter's atmosphere down to a few hundred bars. The shallower layers (closer to the surface) show colder than the background temperature anomalies, whereas the deepest layers show warmer than the background anomalies [19]. The structure and magnitude of the brightness temperature suggest a sign inversion of the temperature anomaly, which is consistent with a mass dipole where the density anomaly changes sign accordingly, with denser fluid closer to the surface and less dense at depth.

The total mass variation associated with the GRS is obtained by integrating the density anomaly profile over the horizontal coordinates (θ and ϕ) and along depth (r), from the surface until the density anomaly changes sign. The mass parameter associated with the positive and negative masses (ΔGM) amounts to about 0.126 km^3s^{-2} for H=300 km and 0.965 km^3s^{-2} for H=1,000 km. The peak positive and negative densities are separated by a radial distance denoted hereafter as d. The parameter d is different from the scale height H,

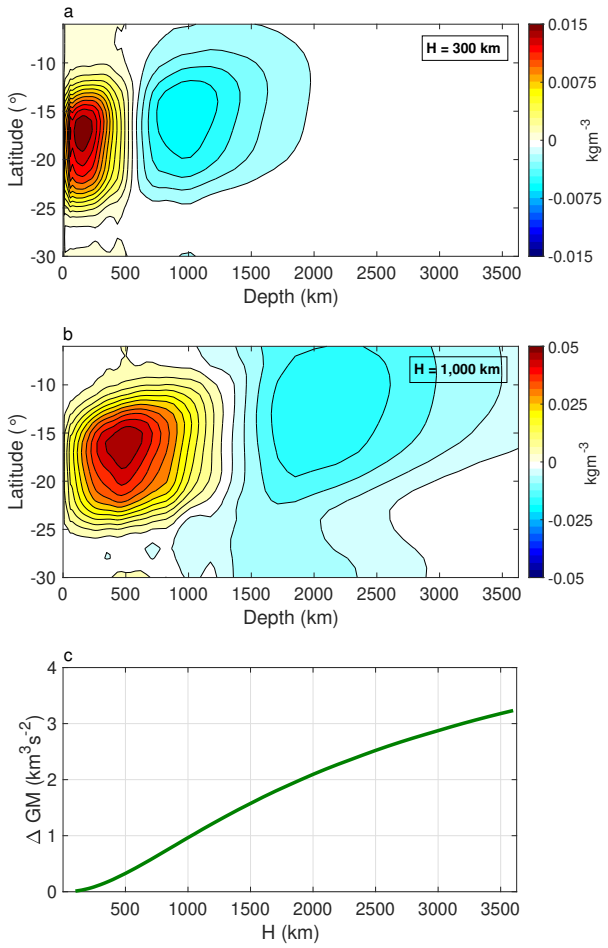

Figure 2: Panels a and b: density anomalies at the GRS location at different vertical levels, derived from the TW equation. The profiles are functions of depth and latitude, for a wind scale height of 300 km (panel a) and 1,000 km (panel b). The density profiles can be compared to mass dipoles featuring a positive density anomaly at the surface and a negative density anomaly at depth. Panel c: mass anomaly ΔGM associated with each mascon constituting the GRS, as a function of the scale height H.

which represents instead the e-folding factor of the exponential decay. Their relationship is unique as to one value of H corresponds one and only one value of d. The radial separation is about 740 km for a dipole of scale height 300 km and 1,600 km for a dipole of scale height 1,000 km. For any value of H, the radial distance d is always larger. The total integrated mass anomaly is close to zero, which is consistent with the requirement that the total mass of Jupiter remains constant. However, this condition is better satisfied for smaller values of the scale heights, whereas deeper GRS models show a residual mass, albeit small (less than 20%). The gravitational effect of the concentrated masses on the Juno spacecraft is non-null because of the radial separation between the two anomalies. Since d is small compared to the planet's radius (less than 1.5% of Jupiter's radius in the cases considered in the study) and the mascon masses are equal but opposite, to first order we can assume that the position of Jupiter's center of mass does not shift. Panel c of Figure 2 shows the GRS mass variation associated with the positive and negative masses (ΔGM) as a function of the scale height H. For scale heights smaller than 1,000 km the mass increases more than linearly with H, whereas for larger values the trend is less than linear. There is a unique relationship between the mass involved in the GRS dynamics and its depth, hence the determination of the positive and negative masses entails the estimation of its scale height.

In view of the results shown in Fig 2, the GRS is modeled in the orbit determination software as a pair of flat disk mascons of radius R and separated by a radial distance d (Figure 3). The positive disk mascon (A) lies closer to the reference ellipsoid at the GRS location. The negative disk mascon (B) is located at the same longitude and latitude but deeper. The two mascons are constrained to have the same mass and opposite sign: GM_A=-GM_B. The radius of the disk mascons is R=8,000 km, so that the circular area of the GRS is similar to the recently observed one [28, 26].

From an orbit determination point of view, the GRS mass anomalies can be modeled using different approaches. For instance one could use a single mascon as in Null [22], two or more mass concentrations located at different latitudes,

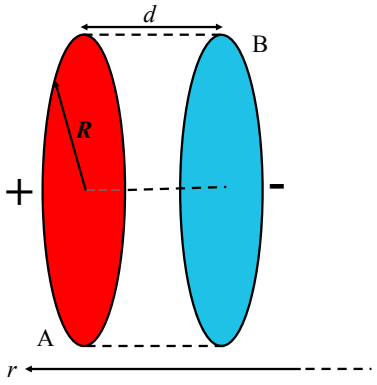

Figure 3: Sketch of the GRS model in the orbit determination code. The pair of disk mascons (A and B) is characterized by the radius R, the masses GM_A and GM_B, and are separated radially by d. The Jovian radial coordinate r points outwards from the center of the planet.

spherical harmonics or Slepian functions. All options are viable and might lead to the detection of the GRS gravity signal. However, in order to infer the depth of the GRS by determining its mass, it is necessary to make assumptions on the density distribution below the visible cloud tops. The choice to model the GRS density anomalies as a pair of concentrated masses at different altitudes is primarily based on the TW equation which can be used to predict the density distribution starting from wind profiles (Figure 2, panels a and b), as demonstrated in Kaspi et al. [17] and Iess et al. [11]; and on Juno MWR observations of brightness temperature anomalies, which undergo a sign inversion as a function of depth [19]. Generally speaking, measurements of the gravity field of planetary bodies are afflicted by non-uniqueness, since a variety of density profiles can fit the same observations. Yet, we can rely on physical considerations in order to choose among the space of possible models. We will discuss the effect of potential mis-modeling of the GRS density anomalies on the orbit determination process in Section 4.

In Figure 4 we compare the gravitational potential along the Juno trajectory during a close GRS overflight for: i) the Finite Element (FE) model of the density anomalies as shown in Fig. 2, for H=300 km (panel a), by considering

each element of the three-dimensional grid as a point mass; ii) the vertical dipole model using disk mascons, from the mathematical formulation in Lass & Blitzer [18]. We find that both potentials follow a similar power law of the distance r' between the spacecraft and the GRS. When sufficiently distant from the dipole, the potential varies like $(r')^{-2}$, whereas when closer to the concentrated masses, the spacecraft senses the closer positive mass and the power law is closer to $(r')^{-1}$. The potential from the FE model is slightly asymmetrical with respect to the time of closest approach between the spacecraft and the center of the GRS, which reflects the slight asymmetry with respect to latitude 20°S in the density distribution (Figure 2, panels a and b). The northward shift of the negative mascon is due to the alignment of u_{cyl} and v_{cyl} with the spin axis, which is neglected in this analysis, as the disk mascon dipole in the radial direction is still a good approximation of the density distribution obtained from the integration of Equation (2), as shown in Figure 4. As the scale height increases beyond 1,000 km, the spacecraft becomes more sensitive to the acceleration due to the positive mass closer to the surface, whereas the signal from the negative mass concentration is no longer detectable and blurs into the background. The gravitational potential differs from that exerted by a dipole and is closer to a gravitational monopole. This effect suggests the presence of a maximum detectable value of H, however this limit is well beyond the scale height range considered in this study (300-1,000 km).

4. Detectability of the GRS with Juno gravity orbits

The Juno spacecraft was inserted in a highly eccentric, quasi-polar orbit around Jupiter in the summer of 2016. The closest approaches to the planet, or perijoves, occur roughly every 53 days (the orbital period). During the overflights, the spacecraft flies over Jupiter's cloud tops down to altitudes as low as 4,000 km. The spacecraft has a limited amount of time to collect data at periapsis, therefore the science orbits have to be optimized for different instruments in order to maximize the scientific return of the mission. The objective of this

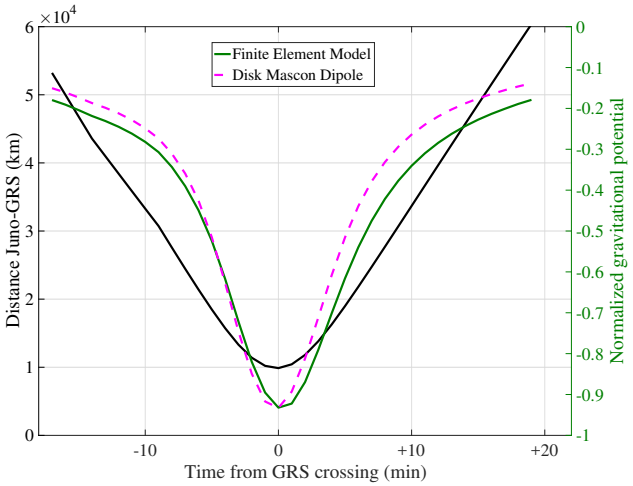

Figure 4: Left y-axis: distance r' between the Juno spacecraft and the GRS during a close overflight (solid black line) as a function of time. Right y-axis: normalized gravitational potential as a function of time for: i) the Finite Element model (solid green line), from the integration of the TW equation; ii) a dipole (dashed magenta line) composed of two disk mascons separated by the distance d (see Figure 3).

work is determining whether it is possible to detect the GRS gravity signal with two targeted Juno gravity passes, using the vertical dipole model. We simulated two-way Doppler data for PJ18 and PJ21, which will occur in 2019 and will use both X- and Ka-band links (7.2-8.4 GHz and 32.5-34 GHz), received and transmitted through the onboard High Gain Antenna (HGA). The Juno spacecraft will fly over the GRS at an altitude of about 13,000 km during PJ18, and slightly over 19,000 km during PJ21. The longitudinal angular distance between the spacecraft and the GRS will be about 10° and 6°, respectively. In addition to the two critical overflights of the GRS, we simulated data for Juno perijoves that were (or, for future ones, that will tentatively be) optimized for gravity measurements: PJ03, PJ06, PJ08, PJ10, PJ11, PJ14, PJ15, PJ17, PJ22, PJ23 and PJ25-PJ33. Although only PJ18 and PJ21 will physically fly over the GRS, including the rest of the gravity passes helps constraining the global gravity field of the planet and the spacecraft state at the beginning of each arc,

which ultimately affect the determination of the GRS mass. The noise level used to simulate the Doppler data was chosen as follows. For perijoves already occurred at the time of our simulations (PJ1 to PJ17), we adopted actual data weights used in the gravity data analysis, between 5 and 10 μms^{-1} (one-way) for an integration time of 60 s. For instance, PJ3 and PJ6 one-way noise level was about 7.5 μms^{-1} [10]. For future perijoves we used data weights ranging between 8-10 μms^{-1} (one-way, 60 s). The noise root mean square (RMS) of Doppler measurements for each perijove depends on several factors. The employment of two independent radio carriers is used to calibrate up to 75% of dispersive noise [2], due to Earth's ionosphere, solar plasma and, specifically for Juno, the Io Plasma Torus [25]. The noise caused by the wet component of Earth's troposphere is accurately calibrated using water vapor radiometers located near the ground antenna [10].

In order to integrate the trajectory of Juno and simulate the radiometric data, we defined a dynamical model to describe the forces acting on the spacecraft, in addition to the GRS mascons already discussed in Section 3. The model included: Jupiter's point mass acceleration from the Jet Propulsion Laboratory (JPL) planetary ephemeris DE438, along with the Sun and the other planets; Jupiter's spin axis position from the latest IAU model [1]; zonal harmonic coefficients from degree 2 to 50, the nominal values for J_2-J_{12} were taken from Iess et al. [10], whereas for higher degrees the nominal value is set to zero; tidal deformations caused by the Galilean satellites up to degree 6, according to Wahl et al. [31]. Other notable accelerations are the point mass accelerations from the main satellites as reported in JPL's satellite ephemeris JUP310; solar pressure, Jupiter's albedo and thermal emission, which require information about the spacecraft structure.

Simulated Doppler data at 60 seconds integration time from all perijoves are combined in a multiarc square-root information filter to estimate parameters of interest. Each element of the solve-for vector influences the recovery of the GRS mascon masses and will be discussed in the following paragraphs. The chosen set of estimated parameters for the numerical simulations is: Jupiter's system

mass parameter (GM) with an *a priori* uncertainty of 2 km^3s^{-2}; pole right ascension and declination (constant term and rate) with *a priori* uncertainties of 10^3 degrees and 10^3 degrees per century, respectively; the precession rate with an *a priori* uncertainty of 10^3 degrees per century; zonal harmonic coefficients J_2-J_{50} with *a priori* uncertainties of 1, harmonic coefficients are adimensional parameters, for reference the unnormalized value of J_2 is of order 10^{-2} for Jupiter [10]; 4x4 tesseral field coefficients with *a priori* uncertainties of 1; the state of the Juno spacecraft at the beginning of each gravity pass with *a priori* uncertainties of 10^9 km for the position and 1 kms^{-1} for the velocity; the tidal Love numbers $k_{m,n}$ when $m+n$ is an even number (up to degree-6), with *a priori* uncertainties of 1, for reference the expected value for k_{22} is close to 0.6 [31]. In addition, we estimate the masses of the two GRS mascons, GM_A and GM_B, with *a priori* uncertainties of $10^2 km^3s^{-2}$ and the constraint of being equal and opposite, as suggested by the TW model. The latter condition implies that only one of the parameters used to define the dipole is estimated independently, given that the correlation coefficient between GM_A and GM_B is imposed to be -1. The filter is used to estimate the mass of one of the mascons while the mass of the opposite concentration is forced to be complementary. Furthermore, the Love numbers $k_{m,n}$ when $m + n$ is an odd number (up to degree-6) are not estimated but included as consider parameters [29], implying that their *a priori* uncertainties (set to 1) and their correlations with the solve-for parameters are taken into account in the definition of the post-fit covariance matrix, but the data strength necessary to estimate them is not available. For a more detailed description of the Jupiter gravity field estimation with Juno see Bolton et al. [3], Folkner et al. [7] and Iess et al. [10].

We will first describe the outcome of the covariance analysis, where the dynamical model used to simulate the Doppler observables along the trajectory of each arc (described in the previous paragraphs) is the same as the one used to calculate the computed Doppler. The differences (residuals) between the simulated observed Doppler and computed Doppler will only show the simulated white noise. The objective is to study the covariance matrix, which contains

information about the formal uncertainties on the estimated parameters and depends on the variability of the Doppler observable with each parameter. Rows 2 and 3 of Table 1 show the expected formal uncertainty (1-sigma) in the estimation of the mascons' masses, GM_A and GM_B for two different simulated values of H. The accuracy achieved with PJ18 alone is 59.5% of the expected mass variation for H=300 km (ΔGM=0.126 km^3s^{-2}), ruling out the possibility of detecting a shallow GRS with a single flyby, since the estimated mascon mass is compatible with zero well within the 3-sigma level. The detectability improves by adding simulated gravity data from PJ21, allowing for the determination of the shallow GRS mass with a relative uncertainty (ratio between σ_{GM} and ΔGM) of 42.9%. If the GRS is deep (H=1,000 km, ΔGM=0.965 km^3s^{-2}), the relative uncertainty is reduced to 5.2% and 3.8% with one and two overflights, respectively. The standard deviation depends on the scale height of the dipole model, specifically, dipoles characterized by a larger radial separation are better resolved in the gravity solution. This can be explained both by the increase in the mass involved in the vortex circulation and by the larger radial separation, which produces a larger dipole moment (product between ΔGM and d) and facilitates the discrimination between the accelerations caused by the two concentrated masses. The estimation accuracies of the other gravity coefficients are not discussed, however we will discuss their influence on the estimation of the dipole mass. The correlation coefficients of the mascon GMs with the other components of the estimated vector are below 0.60. The highest correlations are found with the Love numbers, with a peak of 0.46 for degree-2 coefficients. Since the maximum detectable degree (5) for the Love numbers is already included in the covariance matrix, we study instead the effect of estimating a higher degree tesseral field on the formal uncertainties of the mascon masses. We find that estimating a 5x5 or 6x6 tesseral field degrades the relative uncertainties in Table 1 by less than 5%, pointing to low correlation coefficients with longitudinal variations of the gravity field. Correlations of the mascon parameters with the zonal gravity harmonics are low as well (<0.1). Finally, we report that the estimation errors (differences between simulated and estimated values) are below

	GRS Perijove	**Altitude** (km)	σ_{GM} (km^3s^{-2})		σ^{rel}_{GM} (%)		ϵ_{GM} (km^3s^{-2})		σ_H (km)	
			H		H		H		H	
			300km	1,000km	300km	1,000km	300km	1,000km	300km	1,000km
COV	PJ18	13,000	0.075	0.050	59.5	5.2	0.064	0.077	105	40
	PJ18 & PJ21	13,000 & 19,000	0.054	0.037	42.9	3.8	0.004	0.074	70	30
REC	PJ18	13,000	0.090	0.052	71.4	5.4	0.114	0.026	135	45
	PJ18 & PJ21	13,000 & 19,000	0.057	0.034	45.2	3.5	0.030	0.133	75	35

Table 1: Simulation results of the detection of the GRS gravity signal for the covariance (rows 2 and 3) and recovery (rows 4 and 5) analyses, considering one or two GRS overflights. The table shows the formal uncertainties, relative uncertainties, estimation errors on the mascon masses (GM_A and GM_B)and formal uncertainty on the scale height H for the shallow (H=300 km) and deep (H=1,000 km) cases.

the 3-sigma level for all the components of the solve-for vector. The uncertainty on the scale height of the GRS in Table 1 (last column) is derived from the estimation of the mascon masses as:

$$\sigma_H^2 = \left(\frac{\partial H}{\partial GM}\right)^2 \sigma_{GM}^2 \tag{3}$$

where $\frac{\partial H}{\partial GM}$ is the inverse of the derivative of the curve in panel c of Fig. 2, calculated at the estimated ΔGM. The smaller formal uncertainties on H for deeper cases is explained by the slope of the curve in Figure 2 (panel c) being steeper around 1,000 km than around 300 km. However, since the curve becomes flatter after 1,000 km, we expect the formal uncertainty on H to increase after this value.

The scale height that characterizes the GRS and is used in the dynamical model varies according to the estimated mass of the mascons and hence affects the formal uncertainties. In fact, the number of overflights of the vortex do not provide the necessary data strength to estimate independently both masses and separation of the mascons. However, these parameters are uniquely related by the TW equation and one (e.g. scale height) can be inferred from the other (e.g. the mass). In order to explore the relationship between estimated mass and scale height, we performed a recovery analysis, where the simulated scale height for the GRS is different from the initial guess used to generate the com-

puted observables. For instance, we simulated tracking data for PJ18 and PJ21 assuming a GRS scale height of 300 km, a ΔGM of 0.126 $km^3 s^{-2}$ (Figure 2, panel b) and a radial separation of 740 km. Our goal is to determine whether it is possible to recover the simulated value for the scale height, which can fit the simulated Doppler data to the noise level. We start from a first-guess scale height of 1,000 km, a ΔGM of 0.965 $km^3 s^{-2}$ and a radial distance of 1,600 km. Unlike the covariance analysis, the Doppler residuals will now show dynamical signatures due to the slightly different accelerations exerted on the spacecraft by the different mascon models. The new estimated value for the mascon masses is (0.122 $\pm$ 0.037) $km^3 s^{-2}$, which corresponds to a smaller scale height of (295 $\pm$ 45) km, closer to the simulated value. For the following iteration, we change accordingly the value of ΔGM and d used in the dynamical model for the trajectory integration. After re-integrating the trajectory, the new estimate for the mascon masses is (0.234 $\pm$ 0.061) $km^3 s^{-2}$, corresponding to a scale height of (415 $\pm$ 65) km. The recovered value of H oscillates around the simulated value and the process is repeated until the simulated Doppler data is fitted to the noise level and until the delta solution for the mascon ΔGM is smaller than the formal uncertainty. After a small number of iterations, the converged estimate for the mascon mass is $\overline{\Delta GM}$=(0.156 $\pm$ 0.057) km^{3}s^{-2}, which corresponds to an estimated $\bar{H}$=(330 $\pm$ 75) km (from Fig. 2, panel c) and is compatible at the 1-sigma level to the value used to simulate the data. The underlying assumption is that, whereas the location of the GRS varies in the dynamical model for PJ18 and PJ21 to match the predictions, its size, mass and overall structure remains constant throughout the simulation time (February-July 2019). The recovery analysis can be repeated inverting the simulated and first guess values, considering only PJ18 or both PJ18 and PJ21. The results are reported in rows 4 and 5 of Table 1 and show that the formal and relative uncertainties on the estimated scale height are degraded by 30% at most in the single-flyby scenario and by 15% at most in the two-flyby scenario in comparison to the covariance analysis, due to their dependence on the scale height used in the dynamical model. The estimation errors in the recovery of the mascon masses are within

the 3-sigma level, with the exception of the deep, PJ18+PJ21 case, whose error is about 4 times the formal uncertainty.

Lastly, we discuss the effect of mis-representing the number and/or location of the concentrated masses constituting the GRS. In our first test we simulated Doppler data using a vertical dipole with a scale height of 300 km, whose gravitational potential is a good approximation of that from the density profile distribution in panel a of Fig. 2. We are interested in determining whether it is possible to fit the simulated Doppler data with a different model for the GRS. To this end, we integrated the trajectory using a single mascon (point mass or disk) located at the GRS latitude and longitude and lying on the cloud top. We used the set of solve-for parameters described at the beginning of Section 4, with the exception of estimating only one mascon mass. We found that even after a considerable number of iterations, the single mascon model is not able to fit the simulated data to the noise level, with Doppler residuals showing dynamical signatures of order 38 μms^{-1}, 4 times larger than the simulated noise RMS. Similarly, when simulating data using a single mascon and trying to reconstruct the trajectory of the spacecraft using a vertical dipole model, we find that it is not possible to fit flat the simulated Doppler data. The data simulation process for the second test considered a horizontal mascon dipole with two masses (point mass or disk) whose magnitude is equivalent to the shallow case (Fig. 2, panel a), but located at different latitudes (deparated by 10°) around the GRS location, rather than at different depths. We tried to fit the simulated data using a vertical mascon dipole and found that the Doppler residuals showed ample dynamical signatures peaking at 40 μms^{-1}, even after a significant number of iterations.

5. Discussion and conclusion

In this work we describe a novel method for the determination of Jupiter's GRS depth with the Juno gravity experiment. This model captures the essential dipole-like structure of the vortex density anomalies, with the advantage

of using one parameter to define it. This translates into a smaller number of parameters to be estimated in the orbit determination process. Doppler data collected during the Juno overflights of the storm are very valuable and sophisticated calibration techniques must be employed in order to reduce the noise on radiometric observables. A smaller set of estimated parameters can make a crucial difference in the detection of the GRS gravity signal because of the limited available data strength [23]. Therefore, our ability to restrict the number of parameters associated with the GRS model is key to successfully determining its depth.

The effect of the GRS dipole on the Doppler residuals that has to be detected in order to infer the depth is very subtle and requires the removal of systematic errors due, for instance, to the ground and onboard instrumentation. Furthermore, other small-scale effects, such as Jupiter's tides and tesseral field, must be included in the dynamical model in order to avoid aliasing of the estimated parameters, although the correlations coefficients are low. Finally, uncertainties on the GRS drift rate might change the conditions of the upcoming overflights by changing the relative longitude between Juno and the GRS.

The results of our simulations show that a detection at the 3-sigma level is possible if the GRS scale height is 300 km or deeper, provided that data from the two gravity overflights of the vortex are combined. We support this by showing that the relative uncertainty on the mascon mass is at least 45% for H larger than 300 km, while the formal uncertainty on the scale height is at least 75 km. These results show a better detectability with a reduced minimum detection depth of the GRS, than what was found in Parisi et al. [23], where only one single flyby of the Juno spacecraft was considered in the analysis and where the estimation of many parameters was required. We also find that the sensitivity of the Doppler data to a different number or location of the mascons is sufficient to discriminate between a vertical dipole, a horizontal dipole or a single mascon model.

Acknowledgments

We thank the Juno Interior and Atmospheric Working Groups for the useful discussions. The research described in this paper was carried out at the Jet Propulsion Laboratory, California Institute of Technology, under a contract with the National Aeronautics and Space Administration (M.P., W.M.F., D.R.B. and K.O.); at the Weizmann Institute of Science in Israel (E.G. and Y.K.); at the Southwest Research Institute under a NASA contract (S.J.B.).

References

[1] Archinal, B.A., A'Hearn, M.F., Bowell, E., Conrad, A., Consolmagno, G.J., Courtin, R. et al. (2010). Report of the IAU Working Group on Cartographic Coordinates and Rotational Elements: 2009. *Celestial Mechanics and Dynamical Astronomy*, 109(2), 101-135.

[2] Bertotti, B., Comoretto, G. & Iess, L. (1993). Doppler tracking of spacecraft with multifrequency links. *Astronomy & Astrophysics*, 269, 608–616.

[3] Bolton, S.J., Adriani, A., Adumitroaie, V., Allison, M., Anderson, J.D., Atreya, S., et al. (2017). Jupiter's interior and deep atmosphere: The initial pole-to-pole passes with the Juno spacecraft. *Science*, 356(6340), 821-825. https://doi.org/10.1126/science.aal2108

[4] Busse, F.H. (1976). A simple model of convection in the Jovian atmosphere, *Icarus*, 29(2), 255-260. https://doi.org/10.1016/0019-1035(76)90053-1

[5] Choi, D.S. & Showman, A.P. (2011). Power spectral analysis of Jupiter's clouds and kinetic energy from Cassini. *Icarus*, 216(2), 597- 609. https://doi.org/10.1016/j.icarus.2011.10.001

[6] Dowling, T.E. & Ingersoll, A.P. (1988). Jupiter's Great Red Spot as a Shallow Water System. *Journal of Atmospheric Science*, Vol. 46(21), 3256-3278. https://doi.org/10.1175/1520-0469(1989)046<3256:JGRSAA>2.0.CO;2

[7] Folkner, W.M., Iess, L., Anderson, J.D., Asmar, S.W., Buccino, D.R., Durante, D., Feldman, M., et al. (2017). Jupiter gravity field estimated from the first two Juno orbits. *Geophysical Research Letters*, 44(10), 4694-4700. https://doi.org/10.1002/2017GL073140

[8] Galanti, E., Kaspi Y. & Tziperman, E., (2017). A full, self-consistent, treatment of thermal wind balance on fluid planets. *Journal of Computational Physics*, 810, 175-195. https://doi.org/10.1017/jfm.2016.687

[9] Galanti, E., Durante, D., Finocchiaro, Iess L. & Kaspi, Y. (2017). Estimating Jupiter's Gravity Field Using Juno Measurements, Trajectory Estimation Analysis, and a Flow Model Optimization. *The Astronomical Journal*, 154(1), https://doi.org/10.3847/1538-3881/aa72db

[10] Iess, L., Folkner, W.M., Durante, D., Parisi, M., Kaspi, Y., Galanti, E., Guillot, T., et al. (2018). Measurement of Jupiter's asymmetric gravity field. *Nature*, 555, 220-222. https://doi.org/10.1038/nature25776

[11] Iess, L., Militzer, B., Kaspi, Y., Nicholson P., Durante D., Racioppa, P. et al. (2019). Measurement and implications of Saturn's gravity field and ring mass. *Science*, 17 January 2019. https://doi.org/10.1126/science.aat2965

[12] Ingersoll A.P. & Pollard D. (1982). Motion in the interiors and atmospheres of Jupiter and Saturn: Scale analysis, anelastic equations, barotropic stability criterion, *Icarus*, 52(1), 62-80. https://doi.org/10.1016/0019-1035(82)90169-5

[13] Jacob, T., Wahr, J., Pfeffer W.T. & Swenson S. (2012). Recent contributions of glaciers and ice caps to sea level rise, *Nature*, 482, 514-518. https://doi.org/10.1038/nature10847

[14] Kaspi, Y., Flierl, G.R. & Showman, A.P. (2009). The deep wind structure of the giant planets: Results from an anelastic general circulation model. *Icarus*, 202(2), 525-542. https://doi.org/10.1016/j.icarus.2009.03.026

[15] Kaspi, Y., Hubbard, W.B., Showman, A.P. & Flierl, G.R. (2010). The gravitational signature of Jupiter's internal dynamics. *Geophysical Research Letters*, Vol. 37(1), L01204. https://doi.org/10.1029/2009GL041385

[16] Kaspi, Y. (2013). Inferring the depth of the zonal jets on Jupiter and Saturn from odd gravity harmonics. *Geophysical Research Letters*, Vol. 40(4), 676-680. https://doi.org/10.1029/2012GL053873

[17] Kaspi, Y., Galanti, E., Hubbard, W.B., Stevenson, D.J., Bolton, S.J., Iess, L., Guillot, T., et al. (2018). Jupiter's atmospheric jet-streams extend thousands of kilometers deep. *Nature*, 555, 223-226. https://doi.org/10.1038/nature25793

[18] Lass, H. & Blitzer, L. (1982). The gravitational potential due to uniform disks and rings. *Celestial mechanics*, 30(3), 225-228. https://doi.org/10.1007/BF01232189

[19] Li, C., Oyafuso, F.A., Brown, S.T., Atreya, S.K., Orton, G.S., Ingersoll A.P. & Janssen M.A. (2017). How Deep is Jupiter's Great Red Spot? Paper presented at American Geophysical Union Fall Meeting 2017, American Geophysical Union, New Orleans, Louisiana, USA.

[20] Morales-Juberias R. & Dowling, T.E. (2013). Jupiter's Great Red Spot: Fine-scale matches of model vorticity patterns to prevailing cloud patterns. *Icarus*, 225(1), 216-227. https://doi.org/10.1016/j.icarus.2013.03.026

[21] Muller, P.M. & Sjogren, W.L.(1968). Mascons: Lu-

nar Mass Concentrations. *Science*, 161(3842), 680-684. https://doi.org/10.1126/science.161.3842.680

[22] Null, G. W. (1976). Gravity field of Jupiter and its satellites from Pioneer 10 and Pioneer 11 tracking data, *The Astronomical Journal*, 81, 12, 1153-1161. https://doi.org/10.1086/111999

[23] Parisi, M., Galanti, E., Finocchiaro, S., Iess, L. & Kaspi, Y. (2016). Probing the depth of Jupiter's Great Red Spot with the Juno gravity experiment. *Icarus*, 267, 232-242. https://doi.org/10.1016/j.icarus.2015.12.011

[24] Pedlosky, J. (1987). Fundamentals: The Thermal Wind. In *Geophysical Fluid Dynamics* (pp. 42-43). Springer-Verlag, New York, Heidelberg, Berlin. https://doi.org/10.1007/978-1-4684-0071-7

[25] Phipps, P.H., Withers, P., Buccino, D.R, Yang, Y.-M. (2018). Distribution of Plasma in the Io Plasma Torus as Seen by Radio Occultation During *Juno* Perijove 1. *Journal of Geophysical Research Space Physics*, 123(8), 6207-6222. https://doi.org/10.1029/2017JA025113

[26] Sànchez-Lavega, A., Hueso, R., Eichsätdt, G., Orton, G.S., Rogers, J., Hansen, C.J., Momary, T., et al. (2018). The Rich Dynamics of Jupiter's Great Red Spot from JunoCam; Juno Images. *The Astronautical Journal*, 156(4). https://doi.org/10.3847/1538-3881/aada81

[27] Schneider, T. & Liu, J. (2009). Formation of jets and equatorial superrotation on Jupiter. *Journal of the Atmospheric Sciences*, 66, 579-601. https://doi.org/10.1175/2008JAS2798.1

[28] Simon, A.A., Tabataba-Vakili, F., Cosentino, R., Beebe, R.F., Wong M.H. & Orton, G.S. (2018). Historical and Contemporary Trends in the Size, Drift, and Color of Jupiter's Great Red Spot. *The Astronautical Journal*, 155(4). https://doi.org/10.3847/1538-3881/aaae01

[29] Tapley, B.D., Schutz, B.E. and Born G.H. (2004). Consider Covariance Analysis in Statistical Orbit Determination. Elsevier Inc. San Diego, CA, USA.

[30] Vasavada, A.R. & Showman, A.P. (2005). Jovian atmospheric dynamics: An update after Galileo and Cassini. *Reports on Progress in Physics*, 68(8), 1935- 1996. https://doi.org/10.1088/0034-4885/68/8/R06

[31] Wahl, S.M., Hubbard W.B. & Militzer, B. (2016). Tidal response of preliminary Jupiter model. *The Astrophysical Journal*, 831(14). https://doi:10.3847/0004-637X/831/1/14

[32] Yano, J. & Flierl, G.R. (1994). Jupiter's Great Red Spot: compactness condition and stability. *Annales Geophysicae*, 12(1), 1-18. https://doi.org/10.1007/s00585-994-0001-z

[33] Zuber, M.T., Smith, D.E., Watkins, M.M., Asmar, S.W., Konopliv, A.S., Lemoine, F.G., Melosh, H.J., Neumann, G.A., Phillips, R.J., Solomon, S.C., Wieczorek, M.A., Williams, J.G., Goossens, S.J., Kruizinga, G., Mazarico, E., Park, R.S. & Yuan,D.-N. (2013). Gravity Field of the Moon from the Gravity Recovery and Interior Laboratory (GRAIL) Mission. *Science*, 339(6120), 668-671. https://doi.org/10.1126/science.1231507